Research Square

Preprints are preliminary reports that have not undergone peer review.
They should not be considered conclusive, used to inform clinical practice,
or referenced by the media as validated information.

# Precoordination-directed synthesis of high-entropy perovskite colloidal nanocrystals

**Yu Hou**

yhou@ecust.edu.cn

East China University of Science and Technology https://orcid.org/0000-0003-1691-7561

**Wenbo Tan**

East China University of Science and Technology

**Xinyi Liu**

East China University of Science and Technology

**Guocan Chen**

East China University Of Science and Technology

**Xing Wang**

East China University of Science and Technology

**Yu Peng**

East China University of Science and Technology

**Da Liu**

East China University of Science and Technology

**Kuan Xue**

East China University of Science and Technology

**Jialu Yu**

East China University of Science and Technology

**Yilin Xu**

East China University of Science and Technology

**Haiyang Yuan**

East China University of Science and Technology

**Shuang Yang**

East China University of Science and Technology https://orcid.org/0000-0002-8244-3002

**Huagui Yang**

East China University of Science and Technology https://orcid.org/0000-0003-0436-8622

**Article**

**Keywords:**

**Posted Date:** November 9th, 2026

**DOI:** https://doi.org/10.21203/rs.3.rs-11348610/v1

**License:** This work is licensed under a Creative Commons Attribution 4.0 International License.
Read Full License

**Additional Declarations:** There is **NO** Competing Interest.

# Precoordination-directed synthesis of high-entropy perovskite colloidal nanocrystals

Wenbo Tan[1], Xinyi Liu[1], Guocan Chen[1], Xing Wang[1], Yu Peng[1], Da Liu[1], Kuan Xue[1], Jialu Yu[1], Yilin Xu[1], Haiyang Yuan[1], Shuang Yang[1*], Hua Gui Yang[1*], Yu Hou[1*]

[1]Key Laboratory for Ultrafine Materials of Ministry of Education, Shanghai Engineering Research Center of Hierarchical Nanomaterials, School of Materials Science and Engineering, East China University of Science and Technology, Shanghai 200237, China.

[*]Correspondence: syang@ecust.edu.cn (S. Y.); hgyang@ecust.edu.cn (H. G. Y.); yhou@ecust.edu.cn (Y. H.)

## Abstract

Perovskite nanocrystals (PNCs) are solution-processable quantum materials with defect tolerance, tunable electronic structures and strong light-matter interactions, enabling applications in optoelectronics and photocatalysis. Integrating high-entropy configurations into PNCs unlocks a vast chemical space for multicomponent synergy and functional expansion beyond conventional stoichiometry. However, their synthesis has been fundamentally constrained by mismatched multi-precursor kinetics and a trade-off between entropic stabilization and enthalpic phase segregation. Here we report a precoordination-directed strategy for the colloidal synthesis of high-entropy vacancy-ordered double perovskite nanocrystals with high phase purity, near-equimolar stoichiometry and elemental homogeneity. We show that the participation of excess chloride energetically encourages the formation of well-defined metal-halide octahedral units in the precursor, thereby promoting the topological conversion to a high-entropy double-perovskite phase after hot-injection. The elemental synergy of high-entropy PNCs renders them versatile catalysts, delivering ~14-fold improvement in photocatalytic coupling of benzyl alcohol to hydrobenzoin, ~17-fold in oxidative coupling of methane to ethane, and ~35-fold in oxidation of toluene to benzaldehyde, relative to their low-entropy analogues.

## Introduction

Halide double perovskites are gaining attention as lead-free alternatives in optoelectronic[1–3] and photocatalytic[4–6] applications due to their structural stability, chemical robustness[7], and compositional tunability[8]. The recent discovery of high-entropy double perovskites (HEDPs)[9–11], wherein five or more distinct metal cations share a single crystallographic sublattice, has opened an unprecedented compositional space towards material discovery[12], property optimization[13], and advanced applications[14–16]. For instance, the co-existence of multiple octahedra in perovskites brings forth unique energy transfer interactions between confined exciton states, tailored multichannel luminescence, and improved structural stability that cannot readily be achieved in their low-entropy counterparts[17].

The availability of stable colloidal solutions of HEDP nanocrystals (NCs) would enable unique optoelectronic properties and novel device architectures that can further enhance the performance in sensors[18], catalysis[19], and light-emitting devices[20,21]. While low-entropy perovskite NCs can be synthesized through hot-injection[22–24] or reprecipitation[25,26] in a well-controlled manner, the synthesis of nanoscale HEDP-NCs, to our knowledge, has not yet been reported. The major impediment for the synthesis of high-entropy materials lies in the chemical complexity of the multielement system, wherein the competition between enthalpy and entropy often causes immiscibility and phase segregation[27,28]. In solution-phase synthesis of high-entropy NCs synthesis, the formation process is further complicated by the poorly understood interactions between ligands, solvents, and precursors[29]. Large discrepancies in solubility, reactivity, and coordination behavior of different precursors usually yield undesirable precipitation, secondary phases or amorphous products[30], which challenge the production of HEDP-NCs.

In this work, we propose a precoordination-directed strategy for synthesizing colloidal high-entropy double-perovskites nanocrystals with compositional homogenization. We find that the multi-element precursors cannot transform into perovskite crystals during

synthesis, while the pre-incorporation of halide anions can effectively suppress the entropy stabilization effect and promote the amorphous-to-crystalline transformation. Elemental synergistic effects endow $Cs_2\{TeSnZrHfPt\}Cl_6$ high-entropy nanocrystals with universally boosted photocatalytic performance over low-entropy $Cs_2TeCl_6$ nanocrystals across three photocatalytic reactions, delivering ~14-, ~17-, and ~35-fold product formation rates for benzyl alcohol (BA) coupling to hydrobenzoin (HB), methane coupling to ethane, and toluene photo-oxidation to benzaldehyde (BAD), respectively.

## Results

### Synthesis and characterization of HEDP-NCs

Vacancy-ordered double perovskite ($Cs_2MCl_6$, M= Te, Sn, Zr, Hf, Pt, Se) is a prototypical phase that can accommodate multiple elements at M site, and can be grown through a mild solution process according to the work by Folgueras et al[9]. We selected $Cs_2MCl_6$ perovskite single crystals (SCs) as the precursor for the colloidal synthesis, whose crystallographic structure and phase-purity of the $Cs_2MCl_6$ SCs were validated by powder X-ray diffraction (XRD) measurements **(Figure S1)**. The hot-injection process in this work involved the dissolution of SCs in $Cs_2MCl_6$ (M= Te, Sn, Zr, Hf, Pt, Se) and the injection of trimethylsilyl chloride (TMS-Cl) at an optimized temperature in the ranges of 373−453 K **(Figure 1a)**. In the presence of Cs, M and Cl elements, we successfully synthesized high-entropy $Cs_2\{TeSnZrHfPt\}Cl_6$ NCs, whose crystal structure and lattice parameters were ascertained by Rietveld refinement analysis of XRD patterns **(Figure 1b and Table S1)**. However, we found that the HEDP-NCs can only be obtained from Cl-containing precursor solutions: when metal acetate **(Figure S2)**, metal oxide **(Figure S3)** and metal nitrate **(Figure S4)** were used as Cl-free precursors, the colloidal products were amorphous and non-luminescent even after injection of excess TMS-Cl. This is strikingly different from the conventional synthetic protocols of PNCs, such as $CsPbX_3$, where only two of the elements are pre-introduced

into the precursors[31,32]. In fact, this method has been shown to be compatible with the synthesis of single metal $Cs_2MCl_6$ perovskites, like $Cs_2ZrCl_6$ NCs[33] **(Figure S5)**. These observations emphasize the critical role of coordination mode and entropy effect in the coordination chemistry and formation mechanism of high-entropy $Cs_2MCl_6$ NCs[27].

Under ultraviolet (UV) illumination, the colloidal $Cs_2\{TeSnZrHfPt\}Cl_6$ solution exhibits bright golden photoluminescence (PL) emission with an emission peak at 580 nm, an emission lifetime of 530.4 ns and a Commission Internationale de l'Eclairage (CIE) chromaticity coordinate of (0.49, 0.48)[34,35] (**Figure 1c, Figures S6 and S7**), corresponding to $Cs_2\{TeSnZrHfPt\}Cl_6$ SCs **(Figure S8)**. The high-entropy enhancement endows the material with long-term PL stability that can maintain its original PL intensity over 20 hours at room temperature in air (**Figure S9**). A high-angle annular dark-field scanning transmission electron microscopy (HAADF-STEM) image of $Cs_2\{TeSnZrHfPt\}Cl_6$ NCs revealed uniform and monodisperse octahedral nanoparticles with an average particle size of 38.1 ± 8.9 nm **(Figures 1d and 1e)**, in agreement with dynamic light scattering (DLS) analysis (35.5 ± 4.9 nm, **Figure 1f**). High-resolution TEM images reveal lattice fringes with a spacing of 0.73 nm that corresponds to the (110) plane of $Cs_2MCl_6$ perovskite[9] **(Figure S10)**. Elemental homogeneity within a single particle was verified by energy-dispersive X-ray spectroscopy (EDS) elemental maps, which show co-localization of Cs, M and Cl signals in the same area **(Figure 1g)**. The pie chart displays similar atomic ratios of Te, Sn, Zr, Hf and Pt **(Figure 1h)**, agreeing with that derived from inductively coupled plasma-optical emission spectroscopy (ICP-OES) **(Figure 1i)** and X-ray photoelectron spectroscopy (XPS) measurements **(Figure S11)**.

**Local coordination environment analysis**

To probe the coordination environment of the HEDP-NCs, X-ray absorption near-edge structure (XANES) measurements were performed, and the results are shown in **Figure 2a**. The Zr K-edge spectra of HEDP-NCs synthesized from metal chlorides resemble that of the HEDP-SCs, whose atomic packings have been systematically investigated

by previous studies. Fourier transformed extended X-ray absorption fine structure (FT-EXAFS) spectra in **Figure 2b** show a first-shell peak at 2.4 Å for both HEDP-NCs and HEDP-SCs, a spectroscopic characteristic of Zr–Cl bonds. The comparable amplitude of both peaks implies a similar average Zr–Cl coordination number. The product synthesized from metal acetates was also measured as a reference. However, the Zr K-edge data of the product synthesized from metal acetates shifted toward higher energy. Despite the presence of excess TMS-Cl in the solution, there is only one primary peak in FT-EXAFS spectra centered at 2.0 Å that can be assigned to Zr–O bonds from acetate molecules. These local coordination structures and bond lengths of two different products are shown in **Figure 2c**. Wavelet transform extended X-ray absorption fine structure (WT-EXAFS) spectra provide further evidence: a distinct Zr–Cl scattering path appears in HEDP-NCs from metal chlorides and HEDP-SCs, whereas only Zr–O coordination is observed in metal acetates and $ZrO_2$ **(Figure 2d)**. The consistency between HEDP-NCs and HEDP-SCs corroborates the similarities in their local structures, including valence state, coordination number and bond length.

**Component engineering in NCs**

Given the substantial advantages conferred by the multiple elemental synergy, we investigated whether this synthetic strategy allows controllable manipulation of the configurational entropy of perovskite NCs. We began by the synthesis of $Cs_2TeCl_6$ NCs with a low $S_{config}$ of only 0R **(Figure 3a)**. After stepwise incorporation of Sn, Zr and Hf elements, the harvested NCs with $S_{config}$ ranging from 0.7R to 1.3R showed remarkable elemental uniformity as determined by both STEM-EDS and ICP-OES measurements **(Figures 3b and 3c)**[36]. Further incorporation of Pt and Se extended the systems into the high-entropy regime ($S_{config} > 1.5R$), while the five or six M-site elements still sustained both spatial homogeneity and balanced stoichiometry in these HEDP-NCs **(Figure S12)**. One notable observation is that the average particle size of the monodisperse NCs is not heavily affected by the elemental numbers and combinations **(Figure S13)**, suggestive of the universality of our synthetic method in regulating perovskite

formation kinetics. XRD patterns of these NCs revealed consistent face-centered cubic (FCC) phase without detectable structural variations **(Figure 3d)**. Under UV illumination, most of the colloidal NCs dispersed in toluene exhibited distinct golden emission **(Figure 3e)**. The excitation-emission mapping and excitation-dependent PL spectra of $Cs_2\{TeSnZrHfPt\}Cl_6$ NCs indicated the existence of a single emission center with linear dependence on excitation power, which belongs to the emissive feature of self-trapped exciton (STE) emission **(Figures S14 and S15)**[37]. The decrease in PL intensity in $Cs_2\{TeSnZrHfPt\}Cl_6$ NCs may be attributable to internal charge transfer according to previous PL studies.

One common issue for HEDP-NCs synthesis is the large discrepancies in solubility, ligand affinity and decomposition kinetics of various metal precursors that result in asynchronous reaction, uncontrolled aggregation, phase separation or persistent amorphous intermediates. However, it should be noticed that the conventional method is suitable for synthesizing of single-component perovskite NCs, such as $Cs_2ZrCl_6$, but fails to produce HEDP-NCs **(Figure S5)**. Phenomenologically, the non-crystalline mixture with Zr, Sn and Hf M-site elements did not convert to perovskite phase after halide injection, which suggests an entropy stabilization effect of the intermediate non-crystalline states[30,38,39].

**Synthetic mechanism**

To further probe the crystallization mechanism, we scrutinized the structural evolution of HEDP precursors of metal chlorides or metal acetates upon the TMS-Cl injection (see experimental details in Supporting information). The atomic ratios of TMS-Cl to metal precursors (Cl:M) are 0~20 for the synthesis. As shown in the XRD patterns of **Figure 4a**, increasing TMS-Cl addition progressively increased the diffraction peak intensity during the precoordination-directed synthesis, verifying the transition from amorphous intermediates to crystalline NCs. In contrast, no observable diffraction peaks can be seen from the XRD patterns of the sediment obtained from metal acetate precursors. TEM characterizations visualized the transformation from non-crystalline

irregular aggregates (~1000 nm) to uniform NCs at a Cl injection ratio of 6 for the samples synthesized from Cl-containing precursors **(Figure 4b)**. Excess Cl input suppressed the HEDP-NCs growth from 1000 nm to 100 nm, which can be regarded as a potential route to controlling NCs size. Such size evolution is also supported by the DLS results: when using Cl-containing precursors, the particle size decreased monotonically from 1000 nm to ~50 nm upon Cl addition **(Figure 4c)**. For the samples synthesized from metal acetates, we obtained micrometer-scale aggregates throughout all samples, and the morphology did not change at a Cl:M ratio of 6, which is equivalent to a chemical stoichiometry of $Cs_2MCl_6$.

We next applied spectroscopic tools, including Raman spectroscopy, ultraviolet−visible (UV−vis) absorption, and PL emission measurements, to track the octahedral lattice dynamics and optical properties during the HEDP-NCs formation. Raman measurements in **Figures 4d** and **4e** showed that weak M–Cl vibrational modes appeared in Cl-precoordinating samples even without TMS-Cl injection, supporting the presence of preorganized M–Cl octahedra in the precursor state. The intensity of all Raman signals improved upon TMS-Cl injection, and gradually saturated at Cl:M ratio of 10, probably because of complete reaction. For the metal acetate precursor system, no M−Cl vibrations can be detected upon excess TMS-Cl addition. Examination of the sediments by EXAFS measurements indicated the dominance of M–O bonds from the carboxylate coordination. Similar phase evolution was also reflected in UV−vis absorption, PL measurements and photographs of synthesis process under UV illumination. **(Figures S16 and S17)**.

To further investigate the impact of entropy on the precursor coordination environment, zirconium acetate was employed as a precursor to synthesize $Cs_2ZrCl_6$ NCs under the same synthetic conditions. We noticed the emergence of Zr–Cl vibrational signals at a Cl:Zr ratio of 8 **(Figures 4d and 4e)**, which substantiated the conversion from Zr−Ac to Zr−Cl coordination. These results lead to the conclusion that the high-entropy precursor environment with multiple M cations imposes large energetic or kinetic

difficulties in amorphous-to-perovskite transition of NCs. Notably, Cl-precoordination incorporates M–Cl bonds in the precursor, and bypasses the thermodynamically unfavorable reaction pathway, providing a robust and reliable approach for the preparation of HEDP-NCs.

The mechanistic pictures for the synthetic process of HEDP-NCs are interpreted in **Figure 4f**. In conventional synthesis, metal acetates remain strongly coordinated to acetate and long-chain ligands, which yields a high entropy to stabilize the intermediate non-crystalline products. This stabilization effect is particularly pronounced when the number of metal elements increases, which resists the structural reorganization and transition to perovskite phase upon TMS-Cl incorporation. By comparison, our pre-coordination route implants Cl elements within the multi-metal composition in the precursor state and gives rise to molecular M−Cl octahedral configurations before hot-injection. In this case, a flattened energetic landscape is anticipated for the amorphous-to-perovskite transition that enables the successful growth of HEDP-NCs. Overall, unlike the synthesis of common low-entropy $CsPbX_3$ and $Cs_2ZrCl_6$ NCs, a structural homology of precursors to perovskite phase is required for the synthesis of HEDP-NCs, which substantially compensates the entropy-stabilization effect of the intermediate states. To gain mechanistic insight into the synthesis, we performed first-principles density functional theory (DFT) calculations on the Zr and HE systems, in which the M site is occupied by Zr and by a random mixture of Zr, Hf, Te, and Sn cations, respectively, to simulate the energy change associated with the transformation from the precursors to perovskite-like phase during the actual reaction. Three distinct acetate-distorted configurations were constructed to represent the reaction pathway **(Fig. S18)**[40]. As shown in **Fig. 4g**, the calculated results show that perovskite-like phase exhibits a lower overall formation energy in the HE system than in the Zr system, indicating that the high-entropy perovskite-like phase is thermodynamically more stable, which consequently renders the subsequent transformation from acetate to chloride coordination more difficult, in good agreement with experimental observations[41].

**Photocatalytic performance**

Compositional synergy in high-entropy materials generally enables exceptional tunability in binding energy for enhanced surface activity and more efficient surface absorption**,** thereby substantially accelerating photocatalytic reaction kinetics **(Figure 5a)**[42,43]. We first applied the as-prepared HEDP-NCs to photocatalytic toluene oxidation reaction, in which toluene is efficiently converted to BAD as the dominant product with remarkable catalytic performance **(Figure 5b)**. We further evaluated the catalytic performance of materials with varying configurational entropy **(Figure 5c)**. Under identical conditions, low-entropy catalysts exhibited limited activity and moderate selectivity, whereas increasing the number of constituent elements leads to the formation of a high-entropy phase with markedly enhanced performance. The $Cs_2${TeSnZrHfPt}$Cl_6$ NCs delivered a BAD formation rate of 10250 μmol $g^{-1}$ $h^{-1}$ with 92% BAD selectivity, representing a ~35-fold increase compared with $Cs_2TeCl_6$ NCs (295 μmol $g^{-1}$ $h^{-1}$ and 62%). The $Cs_2${TeSnZrHfPt}$Cl_6$ NCs also showed excellent stability over five cycles **(Figure S19)** without structural or compositional changes (**Figures S20-22**), confirming robust photochemical stability. We also summarized the recent advances of photocatalytic toluene oxidation (**Figure S23**)[44-67]. Among all catalysts, $Cs_2${TeSnZrHfPt}$Cl_6$ NCs deliver superior performance in terms of product amounts and selectivity.

To further verify the universality of the high-entropy catalytic system, we expanded the photocatalytic experiments to two additional C–C coupling reactions, namely BA photo-coupling to HB **(Figure 5d)** and methane photo-coupling to ethane **(Figure 5f)**. All liquid-phase products were quantified by liquid chromatography with calibrated standard curves **(Figure S24 and S25)**, while gaseous ethane was measured via gas chromatography using standard calibration curves **(Figure S26)**. The $Cs_2${TeSnZrHfPt}$Cl_6$ NCs afforded ~14-fold (170 μmol $g^{-1}$ $h^{-1}$ and 55%, BA coupling to HB) **(Figure 5e)** and ~17-fold (3264 μmol $g^{-1}$ $h^{-1}$ and 92%, methane coupling to ethane) **(Figure 5g)** activity improvements for the two reactions, respectively. These

results confirm that the formation of high-entropy phases universally boosts the catalytic activity across different photocatalytic bond-activation systems. To our knowledge, this is the first demonstration of halide perovskites as photocatalysts for both reactions, with activity and selectivity comparable to state-of-the-art benchmarks (144 μmol $g^{-1}$ $h^{-1}$ and 95%, $Ag_2S$@CdS for BA coupling to HB[68]; 1700 μmol $g^{-1}$ $h^{-1}$ and 85%, BOC/$TiO_2$ for methane coupling to ethane [69]).

Using photocatalytic toluene oxidation as the benchmark reaction, we systematically conducted control experiments to elucidate the inherent correlation between configurational entropy and photocatalytic performance, motivated by the obvious entropy-governed activity differences. The results showed that neither low-entropy double perovskite nanocrystals (LEDP-NCs) **(Figure S27)**, nor medium-entropy double perovskite nanocrystals (MEDP-NCs) **(Figure S28)** exhibit comparable catalytic activity or BAD selectivity, thereby excluding the dominant influence of specific elemental compositions on the catalytic performance. Ultraviolet photoelectron spectroscopy (UPS) spectra **(Figure 5h and Figure S29)** combined with UV−vis spectra **(Figure S30)** further indicated similar valence band positions and bandgap energies for $Cs_2TeCl_6$ and $Cs_2${TeSnZrHfPt}$Cl_6$ NCs[70], suggesting the enhanced photocatalytic performance is unlikely to originate from differences in intrinsic band energetics.

To further understand the influence of high-entropy effect on photocatalytic efficiency, their charge transfer properties were assessed through electrochemical impedance spectroscopy (EIS)[71] **(Figure S31)**. The Nyquist plot unveiled that $Cs_2${TeSnZrHfPt}$Cl_6$ NCs exhibit the smallest semicircle, indicating the lowest charge transfer resistance and thus superior carrier mobility, contributing to the improved photocatalytic activity. $Cs_2${TeSnZrHfPt}$Cl_6$ NCs dispersed in toluene exhibited lower PL intensity **(Figure S32)**[72], combined with the stronger photocurrent responses **(Figure S33)**, further demonstrating that more photogenerated charge carriers accumulate and actively participate in surface reduction reactions. Notably, compared

with the previously measured $Cs_2\{TeSnZrHfPt\}Cl_6$ NCs, the NCs in toluene showed significantly shortened lifetime, indicating rapid charge transfer between NCs and toluene.

*In-situ* attenuated total reflection surface-enhanced infrared absorption spectra (ATR-SEIRAS) **(Figures 5i and 5j)** revealed the appearance of vibrational features associated with methyl C–H bonds (2970 and 2881 $cm^{-1}$), benzene ring modes (1473 $cm^{-1}$) and aldehyde groups (1230 $cm^{-1}$) upon the reaction, which is consistent with the formation of benzaldehyde and benzyl alcohol intermediates **(Figures S34)**. Compared with $Cs_2TeCl_6$ NCs, $Cs_2\{TeSnZrHfPt\}Cl_6$ NCs showed significantly stronger signals, suggesting enhanced adsorption and activation of methyl groups on the surface of $Cs_2\{TeSnZrHfPt\}Cl_6$ NCs, which facilitated C–H bond activation and accelerated reaction kinetics. To gain deeper insights into photocatalytic toluene oxidation, radical trapping experiments were conducted to validate the catalytic mechanism **(Figure S35)**. The addition of superoxide radical ($\cdot O_2^-$) and hole scavengers significantly suppressed the reaction, whereas electron and carbon-radical scavengers nearly completely inhibited the process, highlighting the critical role of photogenerated electrons in initiating $C(sp^3)$–H bond activation. Electron paramagnetic resonance (EPR) measurements further confirmed the formation of carbon-centered radicals under illumination (**Figure S36**). These results have verified the proposed reaction mechanism and emphasized the crucial role of the higher surface activity and surface adsorption obtained through bandgap modulation from high-entropy structure, as well as the faster photogenerated electron transfer, in enhancing the photocatalytic performance.

## Conclusion

In summary, a precoordination-directed synthesis strategy for HEDP-NCs is established by regulating the coordination chemistry of multicomponent precursor systems. We found that the high-entropy caused by multi-component synergy hinders the conversion of colloidal precursors into perovskite phase even under chloride-ride conditions.

However, the pre-incorporation of chloride anions in the colloidal precursors induces self-organized $[MCl_6]^{2-}$ octahedra arrangements, which is a structurally homologous state that reconfigures the crystallization pathway and promotes amorphous-to-crystalline transformation to HEDP-NCs. To our knowledge, this is the first successful synthesis of HEDP-NCs. The as-synthesized NCs enable more efficient surface absorption and faster electron transfer, making the NCs suitable for photocatalytic applications. For instance, the $Cs_2\{TeSnZrHfPt\}Cl_6$ NCs exhibit high phase purity and uniform elemental distribution, delivering a BAD formation rate as high as 10250 μmol $g^{-1}$ $h^{-1}$ with a selectivity of 92% and an approximately 35-fold enhancement in photocatalytic toluene oxidation performance compared to LEDP-NCs. This work underscores the critical role of coordination environment engineering in overcoming entropy-driven limitations in complex systems. The precoordination-directed strategy is expected to be broadly applicable to the synthesis of complex high-entropy nanocrystal materials with tunable compositions and functionalities.

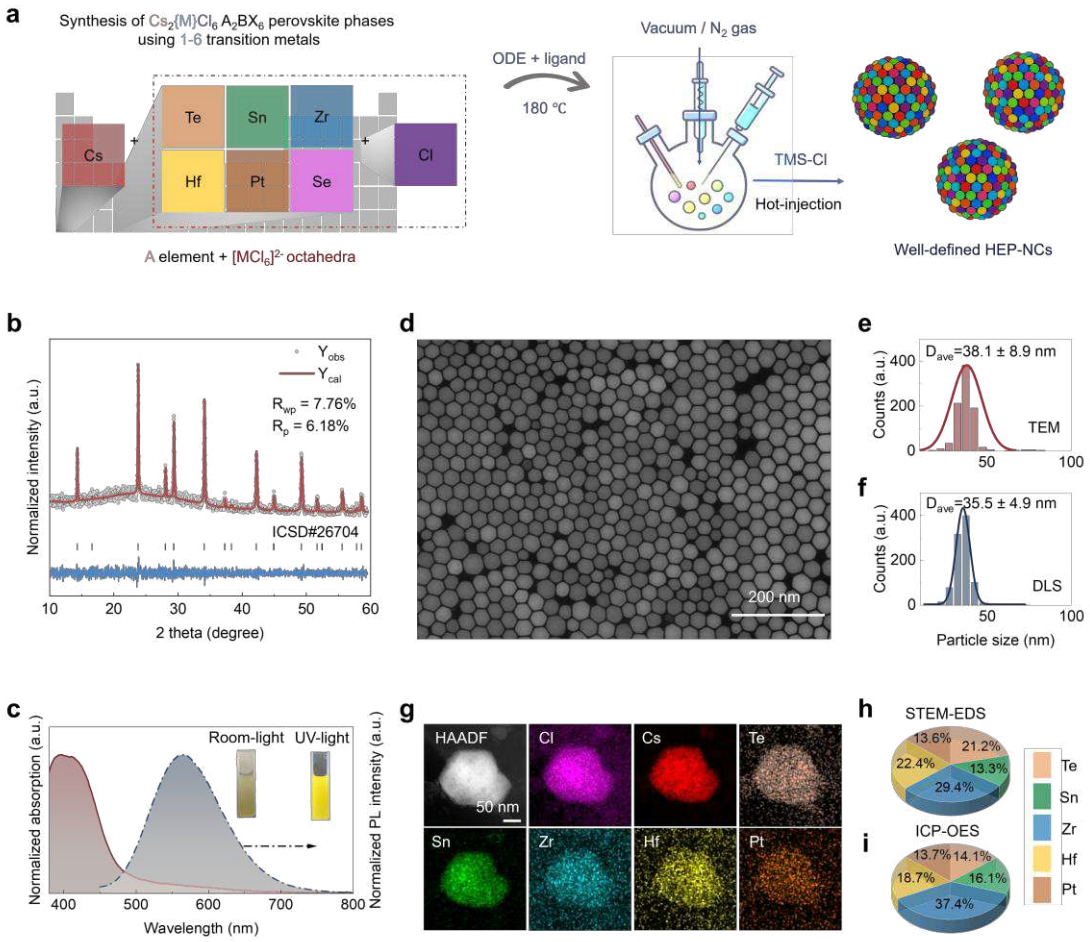



**Figure 1. Synthesis and characterization of high-entropy perovskite NCs.** (a) Schematic illustration of elemental composition and precoordination-directed synthesis of HEDP-NCs. (b) XRD pattern and Rietveld refinement result of $Cs_2\{TeSnZrHfPt\}Cl_6$ NCs. (c) UV−vis absorption and PL spectra of $Cs_2\{TeSnZrHfPt\}Cl_6$ NCs. The insets show photographs of corresponding colloidal solution under room light and UV light (365 nm). (d) TEM image of $Cs_2\{TeSnZrHfPt\}Cl_6$ NCs, exhibiting monodisperse morphology and dimensional uniformity. Particle size distribution statistics of $Cs_2\{TeSnZrHfPt\}Cl_6$ NCs measured by (e) TEM and (f) DLS. (g) HAADF-STEM images and STEM-EDS elemental maps of $Cs_2\{TeSnZrHfPt\}Cl_6$ NCs. The proportion of tetravalent metal elements in $Cs_2\{TeSnZrHfPt\}Cl_6$ NCs obtained from (h) STEM-EDS and (i) ICP-OES measurements.

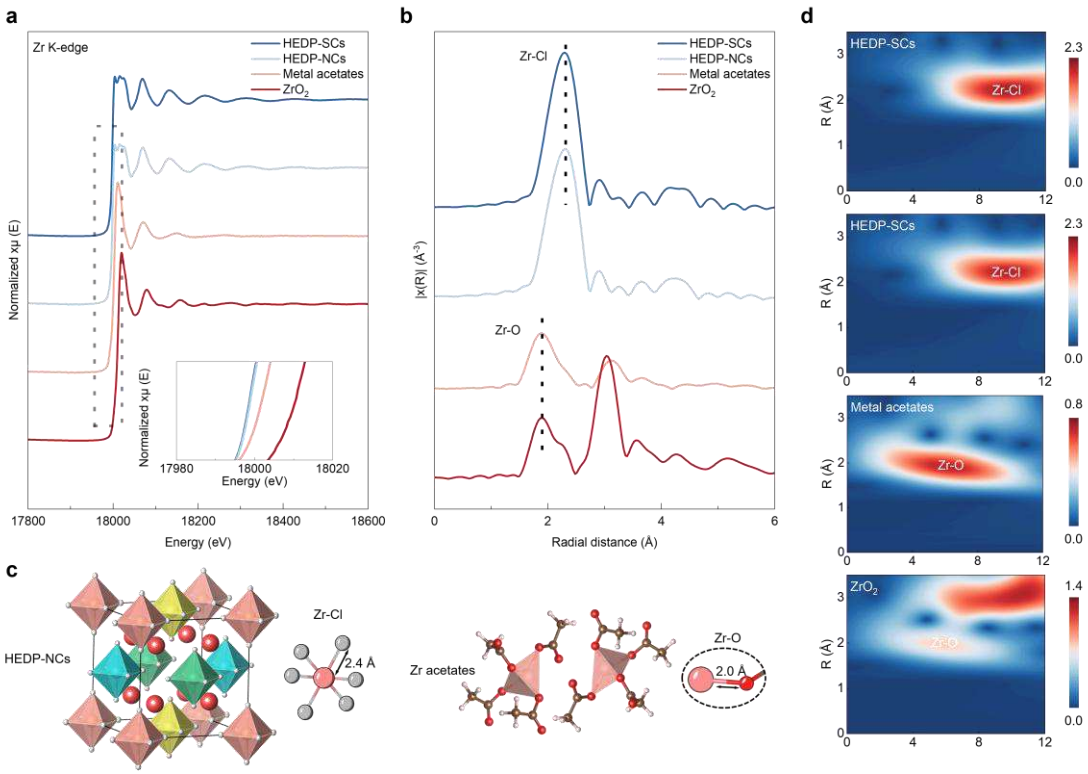



**Figure 2. Local coordination environment of Zr in the resulting products.** (a) Zr K-edge XANES spectra, (b) Zr K-edge FT-EXAFS spectra and (c) schematic diagrams of local structures and bond lengths of the two products. (d) $K^3$-weighted Zr K-edge wavelet transform EXAFS spectra of HEDP-NCs, HEDP-SCs, products synthesized with metal acetates and $ZrO_2$ reference.

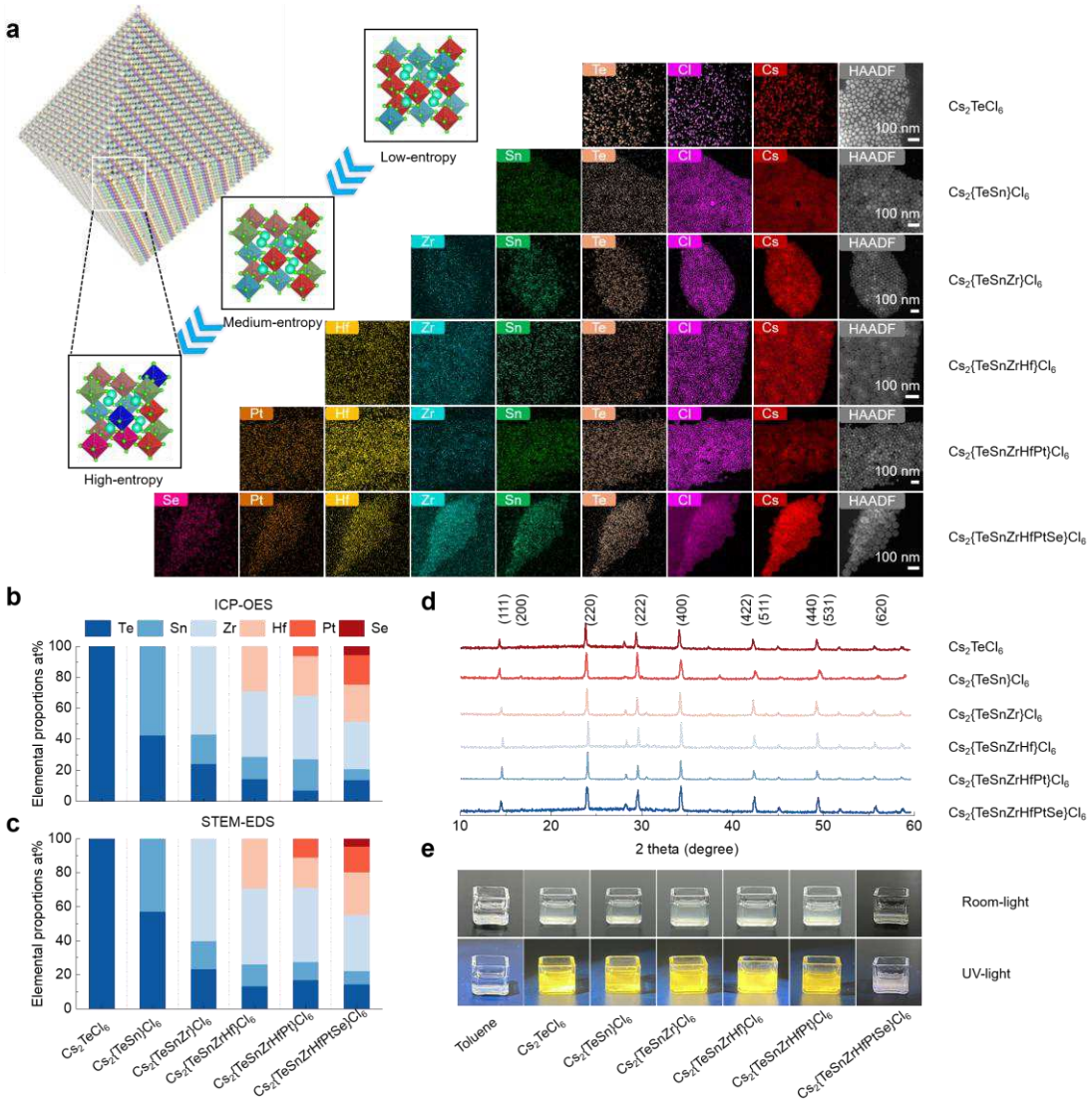



**Figure 3. Component engineering in perovskite NCs.** (a) Conceptual illustration of the transition of $Cs_2MCl_6$ NCs from low-entropy to high-entropy upon M-site doping, and HAADF-STEM images and corresponding EDS elemental maps of LEDP-, MEDP-, and HEDP-NCs. Elemental proportions (at. %) in $Cs_2TeCl_6$, $Cs_2\{TeSn\}Cl_6$, $Cs_2\{TeSnZr\}Cl_6$, $Cs_2\{TeSnZrHf\}Cl_6$, $Cs_2\{TeSnZrHfPt\}Cl_6$ and $Cs_2\{TeSnZrHfPtSe\}Cl_6$ NCs from (b) ICP-OES and (c) STEM-EDS characterizations. (d) XRD patterns of the perovskite NCs. (e) Photographs of colloidal perovskite NCs in toluene under room-light and 365 nm UV light irradiation.

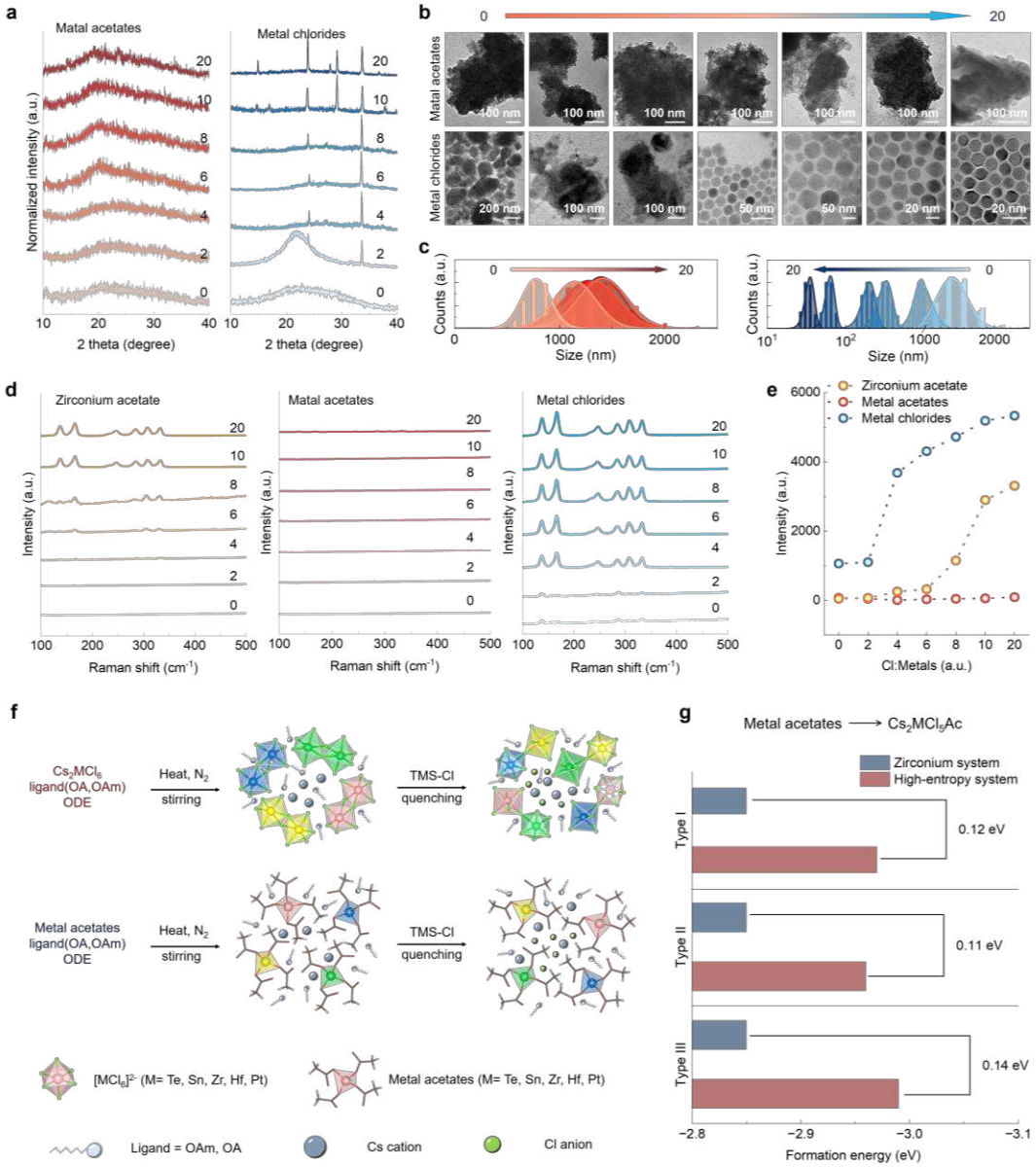



**Figure 4. Synthetic mechanism of high-entropy perovskite NCs.** (a) XRD, (b) TEM and (c) DLS characterizations of products obtained via conventional synthesis and precoordination-directed synthesis routes with different ratios between M and injected Cl elements. (d) Raman spectra of products obtained via metal acetates and metal chlorides and $Cs_2ZrCl_6$ NCs obtained via Zr acetate with increasing chloride concentration and (e) the comparison of Raman intensity. (f) Schematic diagrams of mechanisms for precoordination-directed synthesis and conventional synthesis. (g) Formation energies of perovskite-like phases for Zr and high-entropy (containing Zr, Sn, Te, and Hf) systems using three distinct configurations of metal acetate precursors and calculated by the density functional theory.

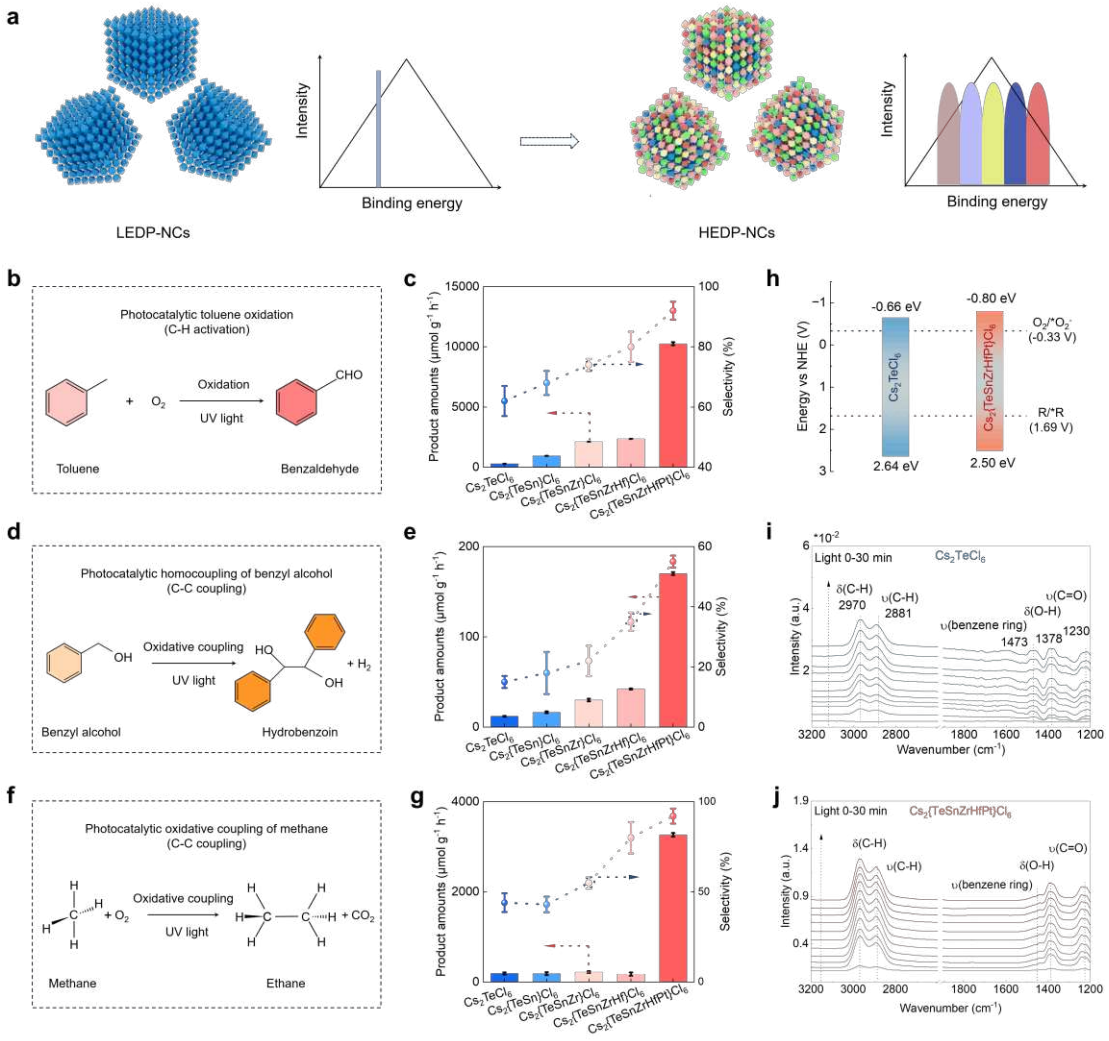



**Figure 5. Photocatalytic performance and mechanism of perovskite NCs.** (a) The comparison of $Cs_2\{TeSnZrHfPt\}Cl_6$ and $Cs_2TeCl_6$ in terms of surface absorption, which is conducive to enhancing the reactivity for three different reactions. (b) and (c) Photocatalytic toluene oxidation equation and performance. (d) and (e) Photocatalytic benzyl alcohol coupling equation and performance. (f) and (g) Photocatalytic methane coupling equation and performance. (h) Band energy levels of $Cs_2TeCl_6$ and $Cs_2\{TeSnZrHfPt\}Cl_6$ NC films. (i) and (j) The comparison of *in-situ* ATR-SEIRAS spectra of $Cs_2TeCl_6$ and $Cs_2\{TeSnZrHfPt\}Cl_6$ NCs in terms of photocatalytic toluene oxidation.

## Methods

### Materials

CsCl (99.9%), $TeCl_4$ (99.9%), $SnCl_4$ (99.9%), $ZrCl_4$ (99.9%), $HfCl_4$ (99.9%), $PtCl_4$ (99.9%), $SeCl_4$ (99.9%), $CH_3COOCs$ (99.9%), $Sn(CH_3COO)_4$ (99.9%), $Zr(CH_3COO)_4$ (99.9%), $Hf(CH_3COO)_4$ (99.9%), $Se(CH_3COO)_4$ (99.9%), $Cs(NO_3)$ (99.9%), $Sn(NO_3)_4$ (99.9%), $Zr(NO_3)_4$ (99.9%), $Hf(NO_3)_4$ (99.9%), $Pt(NO_3)_4$ (99.9%), $Cs_2O$ (99.9%), $SnO_2$ (99.9%), $ZrO_2$ (99.9%), $HfO_2$ (99.9%), $TeO_2$ (99.9%), $PtO_2$ (99.9%), 12 $mol \cdot L^{-1}$ HCl (37.0%), acetonitrile (99.9%), methyl alcohol (99.9%), ethyl alcohol (99.9%), benzoin (99.9%), deoxybenzoin (99.9%), R,S-hydrobenzoin (99.9%), R,R-hydrobenzoin (99.9%), benzaldehyde (99.9%), benzyl alcohol (99.9%) and benzoic acid (99.9%) were purchased from Sigma Aldrich. Trimethylsilyl chloride (TMS-Cl) (99.9%), hexane (99.9%), toluene (99.9%), ethyl acetate (99.9%), oleic acid (OA) (99.7%), oleylamine (OAm) (90.0%), 1-octadecene (ODE) (90.0%) were purchased from Macklin. All the reagents were used as received without further purification.

### Synthetic procedure for $Cs_2TeCl_6$, $Cs_2SnCl_6$, $Cs_2ZrCl_6$, $Cs_2HfCl_6$, $Cs_2PtCl_6$ and $Cs_2SeCl_6$ single crystals

Stoichiometric amounts of $TeCl_4$, $SnCl_4$, $ZrCl_4$, $HfCl_4$ or $PtCl_4$ precursor were dissolved in a vial containing 12 $mol \cdot L^{-1}$ HCl at 350 K, and the stoichiometric amount of CsCl precursor was dissolved in a separate vial containing 12 $mol \cdot L^{-1}$ HCl at 303 K. The CsCl stock solution was then rapidly added to the $TeCl_4$, $SnCl_4$, $ZrCl_4$, $HfCl_4$, $PtCl_4$ or $SeCl_4$ stock solution at 300 K. $Cs_2ZrCl_6$, $Cs_2SnCl_6$, $Cs_2TeCl_6$, $Cs_2HfCl_6$, $Cs_2PtCl_6$ or $Cs_2SeCl_6$ single crystals (SCs), respectively, precipitated immediately from solution. Excess solution was removed, and powders were washed with ethanol, blown by $N_2$ gas and stored under vacuum.

### Growth of the $Cs_2\{TeSnZrHfPtSe\}Cl_6$ SCs

Stoichiometric amounts of $Cs_2TeCl_6$, $Cs_2SnCl_6$, $Cs_2ZrCl_6$, $Cs_2HfCl_6$, $Cs_2PtCl_6$ and $Cs_2SeCl_6$ SCs were dissolved in an uncapped vial containing 5 mL of 12 $mol \cdot L^{-1}$ HCl

at 370 K with stirring at 1,000 rpm for 1 h. Once all powders were dissolved, the stir bar was removed from the solution and the vial returned to the hot plate, which was turned down to 350 K for 1 h. The vial remained uncapped and at 350 K during the entire synthesis process. After the reaction, excess solution was removed, and single crystals were washed with ethanol, blown by $N_2$ gas and stored under vacuum. Other SCs were also synthesized in accordance with the aforementioned process.

**Precoordination-directed synthesis of $Cs_2${TeSnZrHfPtSe}$Cl_6$ nanocrystals**

The $Cs_2${TeSnZrHfPtSe}$Cl_6$ nanocrystals (NCs) were produced by a hot-injection method using a chloride-driven strategy **(Figure 1a)**. In a typical synthesis, 0.1 mmol $Cs_2${TeSnZrHfPtSe}$Cl_6$ SCs were added into a three-neck flask containing ODE (25 mL), OA (1 mL) and OAm (1 mL), and then were heated at 380 K under vacuum conditions for 70 min. After switching the system to a $N_2$ atmosphere, the mixture was heated at 450 K. Then, 2 mL TMS-Cl was swiftly injected by using a preheated glass syringe at 400 K. After a 10 s reaction, the reaction mixture was cooled by the ice-water bath. For purification, the crude solution was washed three times with ethyl acetate and the NCs were redispersed in hexane. Other NCs were also synthesized in accordance with the aforementioned process. Traditional synthesis was applied for NCs to highlight the superiority of chloride-driven synthesis strategy. Stoichiometric amounts of metal acetates, metal oxides and metal nitrate precursors were used, and the remaining synthesis steps were unchanged.

**Material characterization**

The crystallographic information of as-prepared samples was determined by X-ray diffraction (XRD) from Bruker D8 Advanced Diffractometer with Cu Kα radiation (λ = 1.54178, 40 kV, 40 mA) at the scanning speed of 4 °/min. Transmission electron microscopy (TEM) was conducted using Thermo Fisher Talos F200X microscope under 200 kV. High angle annular dark field (HAADF)-STEM images were acquired with a convergence semi-angle of 11 mrad, and inner- and outer-collection angles of 59 and

200 mrad, respectively. Energy dispersive X-ray spectroscopy (EDS) was measured using four in-column Super-X detectors. Attenuated total reflection surface-enhanced infrared absorption spectroscopy (ATR-SEIRAS) spectra were measured using KBr pellets from Thermo Fisher Nicolet 6700 in the range of 3200−1200 $cm^{-1}$. The valence-band maximum and Fermi level were determined by ultraviolet photoelectron spectroscopy (UPS, KRATOS AXIS SUPRA) with He source of incident energy of 21.21 eV (He I line). X-ray photoelectron spectroscopy (XPS) was performed on ESCALAB 250 Xi X-ray photoelectron spectrometer using a monochromatized Al K$\alpha$ X-ray source ($h\upsilon$ = 1486.6 eV) to investigate surface elements content and valence of as-prepared samples. The XPS data were calibrated by the binding energy of C 1s peak at 284.8 eV. Extended X-ray absorption fine structure (EXAFS) and X-ray absorption near edge structure (XANES) at Zr K-edge were measured at room temperature on the 1W1B beamline at the Beijing Synchrotron Radiation Facility (BSRF). Raman spectroscopy was recorded using a Renishaw InVia Reflex confocal Raman spectrometer with a 532 nm laser. Elemental compositions of the NCs were determined by inductively coupled plasma-optical emission spectrometer (ICP-OES) on Zetium. The hydrodynamic diameters of the NCs were collected by dynamic light scattering (DLS) using the Zetasizer Nano ZS system.

**Optical characterization**

Transmittance spectra of the NCs were measured by using a Cary 500 UV–vis–NIR spectrophotometer. Steady-state and time-resolved photoluminescence (PL) and photoluminescence excitation (PLE) spectra were measured using an Edinburgh FLS1000 fluorescence spectrometer.

**Photocatalytic measurements for oxidation of toluene into benzaldehyde**

Typically, 2 mg photocatalyst was dispersed in 5 mL toluene under ultrasonication in a 50 mL quartz reactor. Then the reaction solution was stirred in the dark state for 30 min to achieve dynamic gas dissolution equilibrium. Subsequently, the above mixture was

irradiated with UV light (λ = 365 nm, light intensity of 65 mW $cm^{-2}$, CEL-HXF300, Beijing China Education Au-light Co., Ltd) for 3 h. The reaction system was continuously stirred to ensure uniform irradiation and the temperature was maintained at 25 °C by a circulating air blowing system. After reaction, the suspension was centrifuged at 10000 rpm for 3 min, and the organic products in solution were analyzed by the GC (HPLC, Agilent 1100 equipped with a DAD detector) with a flame ionization detector (FID).

**Photocatalytic measurements for coupling of benzyl alcohol to hydrobenzoin**

Typically, 10 mg photocatalyst was dispersed in the mixture of 10 mL acetonitrile and 50 μL benzyl alcohol under ultrasonication in a 50 mL quartz reactor. Before irradiation, the reactor was evacuated. Then high-purity $N_2$ (99.999 %) was injected as the reaction gas and the reaction solution was stirred in the dark state for 30 min to achieve dynamic gas dissolution equilibrium. Subsequently, the above mixture was irradiated by UV irradiation (λ = 365 nm, light intensity of 65 mW $cm^{-2}$, CEL-HXF300, Beijing China Education Au-light Co., Ltd) for 8 h. The reaction system was continuously stirred to ensure uniform irradiation and the temperature was maintained at 25 °C by a circulating air blowing system. After reaction, the suspension was centrifuged at 10000 rpm for 3 min, and the organic products in solution were analyzed by the GC (HPLC, Agilent 1100 equipped with a DAD detector) with a flame ionization detector (FID), where the photocatalyst is removed by filtration.

**Photocatalytic measurements for oxidative coupling of methane to ethane**

Typically, 5 mg catalyst was dispersed onto a glass fibre filter membrane and fixed in the reactor. The reactor was then purged with a mixture of methane and $O_2$ in a ratio of 70:1 to establish adsorption-desorption equilibrium before testing. A 300 W xenon lamp (Microsolar 300 Xenon lamp, Beijing Perfectlight) was used as the light source. The gas products were analysed using a gas chromatograph (GC-2014, Shimadzu) equipped with two flame ionization detectors (FIDs) and a thermal conductivity detector (TCD).

Hydrocarbon products (for example, ethane) were separated using a capillary column (HP-PLOT/Q, 30 m × 0.53 mm × 40 μm, Agilent) and quantified by external calibration. For the $CO_2$ analysis, the reactor outlet was connected to a gas chromatograph sampling loop, followed by separation on a Porapak Q packed column (2 m × 2 mm, Solution Instrument). The eluted $CO_2$ was then passed through a methanizer unit, where it was quantitatively converted into $CH_4$ and subsequently detected by the FID. The rate of product formation was calculated by dividing the amount of product quantified in the gas mixture by the catalyst mass, and then further dividing by the time required for the gas to pass over the catalyst surface.

The product selectivity was calculated using the following equations:

$$\text{Product amount } (\mu\text{mol g}^{-1}\text{ h}^{-1}) = \frac{\sum \text{moles of corresponding product}}{\text{photocatalyst dosage} \times \text{time}} \quad (1)$$

$$\text{Selectivity} = \frac{\text{Amount of corresponding product}}{\text{Amount of all products}} \times 100\% \quad (2)$$

**Photoelectrochemical measurements**

Before the preparation of photoelectrodes, indium tin oxide (ITO) glass substrates were cleaned sequentially for 15 minutes by soap, deionized water, ethyl alcohol, and acetone in the ultrasonic bath. Then the substrates were treated with ultraviolet ozone for 30 minutes. The NCs solutions were spin-coated on the ITO substrates at 4000 rpm for 30 s. After that, the substrates were annealed at 373 K for 10 minutes. The photoelectrochemical properties were investigated in a three-electrode quartz cell using 0.1 mol·$L^{-1}$ tetrabutylammonium hexafluorophosphate ((TBA)$PF_6$). A platinum mesh, an Ag/AgCl reference electrode (saturated with KCl and protected by a Luggin capillary), and the as-prepared films on ITO substrates were used as the counter electrode, the reference electrode, and the working electrode, respectively. A 300 W Xe lamp (CEL-HXBF 300) was adopted as the light source. Photocurrent responses were measured at 0 V vs. Ag/AgCl reference electrode. Electrochemical impedance spectra (EIS) were recorded at the open-circuit potential with frequencies ranging from $10^{-1}$ to $10^6$ Hz. Electron paramagnetic resonance (EPR) spectra were acquired at room

temperature on a Bruker EMXPlus-6/1 spectrometer.

**Theoretical calculation methods**

The Vienna Ab-initio Simulation Package (VASP)[73] within the projector augmented wave (PAW) formalism[74] is used in the present DFT calculations. The generalized gradient approximation (GGA) for the exchange correlation functional within the Perdew-Burke-Ernzerhof (PBE)[75] parametrization is employed. The kinetic cut-off energy was set to 450 eV and coupled with the projector-augmented wave method. Also, the structure optimizations used a 1 × 1 × 1 Monkhorst–Pack k-point grid. All the atoms were allowed to relax and the convergence criteria for the maximal force on each relaxed atom was less than 0.05 eV/Å. The energy $\Delta E$ of molecule interacting with perovskite was calculated as:

$$\Delta E = E_{\mathrm{Cs_2MCl_5Ac}} - 2E_{\mathrm{CsCl}} - E_{\mathrm{MCl_3Ac}} \quad (3)$$

Where $E_{\mathrm{Cs_2MCl_5Ac}}$, $E_{\mathrm{CsCl}}$ $and$ $E_{\mathrm{MCl_3AC}}$ are the energies of the low-entropy system and the components of the system, respectively. Similarly, the high-entropy system follows the same steps.

## Data availability

All data that support the findings of this study are available in the article and its Supplementary Information.

## Reference


1. Luo, J. *et al*. Efficient and stable emission of warm-white light from lead-free halide double perovskites. *Nature* **563**, 541–545 (2018).

2. Stranks, S. D. & Snaith, H. J. Metal-halide perovskites for photovoltaic and light-emitting devices. *Nat. Nanotech.* **10**, 391–402 (2015).

3. Chen, Q. *et al*. All-inorganic perovskite nanocrystal scintillators. *Nature* **561**, 88–93 (2018).

4. Vesborg, P. C. K. Photocatalysis: hi-time for perovskites. *Nat. Energy* **2**, 16205 (2017).

5. Hansora, D. *et al*. All-perovskite-based unassisted photoelectrochemical water splitting system for efficient, stable and scalable solar hydrogen production. *Nat. Energy* **9**, 272–284 (2024).

6. Li, L. *et al*. Creation of dopant-plasmon synergism in double perovskites for bias-free photoelectrochemical synthesis of bromohydrins and hydrogen peroxide. *Angew. Chem. Int. Ed.* **64**, e202424395 (2025).

7. Cho, H. *et al*. Overcoming the electroluminescence efficiency limitations of perovskite light-emitting diodes. *Science* **350**, 1222–1225 (2015).

8. Volonakis, G. *et al*. Lead-free halide double perovskites via heterovalent substitution of noble metals. *J. Phys. Chem. Lett.* **7**, 1254–1259 (2016).

9. Folgueras, M. C., Jiang, Y., Jin, J. & Yang, P. High-entropy halide perovskite single crystals stabilized by mild chemistry. *Nature* **621**, 282–288 (2023).

10. Oh, S. *et al*. Unveiling entropy-driven performance enhancement in double perovskite oxygen electrodes for protonic ceramic electrochemical cells. *Adv. Energy Mater.* **15**, e03176 (2025).

11. Tang, Y. *et al*. Metal halide perovskite enriched with entropy-induced lattice distortion for enhanced X-ray detection. *ACS Nano* **19**, 30396–30406 (2025).

12. George, E. P., Raabe, D. & Ritchie, R. O. High-entropy alloys. *Nat. Rev. Mater.* **4**, 515–534 (2019).

13. Hsu, W. L., Tsai, C. W., Yeh, A. C. & Yeh, J. W. Clarifying the four core effects of high-entropy materials. *Nat. Rev. Chem.* **8**, 471–485 (2024).

14. Ouyang, B. & Zeng, Y. The rise of high-entropy battery materials. *Nat. Commun.* **15**, 973 (2024).

15. He, Y. *et al*. High entropy superconductors. *Physics Reports* **1144**, 1–44 (2025).

16. Sarkar, A. *et al*. High entropy oxides for reversible energy storage. *Nat. Commun.* **9**, 3400 (2018).

17. Xue, J. *et al*. High-entropy double perovskites with tailored multichannel luminescence. *J. Am. Chem. Soc.* **147**, 47764–47772 (2025).

18. Wieliczka, B. M. *et al*. Nanocrystal-enabled perovskite heterojunctions in photovoltaic applications and beyond. *Adv. Energy Mater.* **13**, 2204351 (2023).

19. Mai, H. *et al*. Synthesis of layered lead-free perovskite nanocrystals with precise size and shape control and their photocatalytic activity. *J. Am. Chem. Soc.* **145**, 17337–17350 (2023).

20. Zhang, L. *et al*. Rapid room temperature entropy-stabilized synthesis enabling super-stable metal halide perovskite semiconductor colloidal nanocrystals. *Adv. Funct. Mater.* **35**, 2423450 (2025).

21. Liu, X. *et al*. High-entropy lead-free organic-inorganic hybrid perovskites exhibiting broad absorption and bright golden emission for LEDs. *Angew. Chem. Int. Ed.* **65**, e16911 (2026).

22. Protesescu, L. *et al*. Nanocrystals of cesium lead halide perovskites ($CsPbX_3$, X = Cl, Br, and I): novel optoelectronic materials showing bright emission with wide color gamut. *Nano Lett.* **15**, 3692–3696 (2015).

23. Liu, B. *et al*. Record high external quantum efficiency of 19.2% achieved in light-emitting diodes of colloidal quantum wells enabled by hot-injection shell growth. *Adv. Mater.* **32**, 1905824 (2020).

24. Yuan, L. *et al*. Quantum-confined dodecahedron $CsPbBr_3$ quantum dots by a sequential post-treatment strategy for efficient blue PeLEDs. *Adv. Funct. Mater.* **32**,

2208065 (2022).

25. Zhang, F. *et al*. Brightly luminescent and color-tunable colloidal $CH_3NH_3PbX_3$ (X = Br, I, Cl) quantum dots: potential alternatives for display technology. *ACS Nano* **9**, 4533–4542 (2015).

26. Wu, L. *et al*. Violet perovskite quantum dots of $MA_3Bi_2Br_9$ and $MA_3Bi_2Br_6Cl_3$ synthesized by the Cb-LARP method with tunable emission wavelengths in range of 379–400 nm. *Adv. Funct. Mater.* **35**, 2415315 (2025).

27. Kar, N. & Skrabalak, S. E. Synthetic methods for high-entropy nanomaterials. *Nat. Rev. Mater.* **10**, 638–653 (2025).

28. Yao, Y. *et al*. High-entropy nanoparticles: synthesis-structure-property relationships and data-driven discovery. *Science* **376**, eabn3103 (2022).

29. Huang, H. *et al*. Growth mechanism of strongly emitting $CH_3NH_3PbBr_3$ perovskite nanocrystals with a tunable bandgap. *Nat. Commun. 8*, 996 (2017).

30. Sun, X. & Sun, Y. Synthesis of metallic high-entropy alloy nanoparticles. *Chem. Soc. Rev.* **53**, 4400–4433 (2024).

31. Xu, K. *et al*. Tuning from quantum dots to magic sized clusters of $CsPbBr_3$ using novel planar ligands based on the trivalent nitrate coordination complex. *J. Phys. Chem. Lett.* **10**, 4409–4416 (2019).

32. Imran, M. *et al*. Benzoyl halides as alternative precursors for the colloidal synthesis of lead-based halide perovskite nanocrystals. *J. Am. Chem. Soc.* **140**, 2656–2664 (2018).

33. Liu, S. *et al*. Efficient thermally activated delayed fluorescence from all-inorganic cesium zirconium halide perovskite nanocrystals. *Angew. Chem. Int. Ed.* **59**, 21925–21929 (2020).

34. Zhang, W. *et al*. Multiphoton-excited upconversion luminescence and amplified spontaneous emission from $Te^{4+}$-doped $Cs_2SnCl_6$ nanocrystals. *ACS Nano* **19**, 18866–18873 (2025).

35. Li, W. *et al*. Shallow-trap perovskite scintillators for high-resolution, ghosting-free X-ray imaging. *Angew. Chem. Int. Ed.* **65**, e4716874 (2026).

36. Rost, C. M. *et al*. Entropy-stabilized oxides. *Nat. Commun.* **6**, 8485 (2015).

37. He, Y. *et al*. Nature of self-trapped exciton emission in zero-dimensional $Cs_2ZrCl_6$ perovskite nanocrystals. *J. Phys. Chem. Lett.* **14**, 7665–7671 (2023).

38. Wang, J. *et al*. High-entropy alloy-enhanced ZnCdS nanostructure photocatalysts for hydrogen production. *Appl. Catal. B Environ.* **362**, 124763 (2025).

39. Liu, Y. H. *et al*. Toward controllable and predictable synthesis of high-entropy alloy nanocrystals. *Sci. Adv.* **9**, eadf9931 (2023).

40. Huang, Y. *et al*. Self-adhesive high-entropy oxide sub-nanowire monolithic electrocatalysts. *Nat. Nanotechnol.* **21**, 850–858 (2026).

41. Zeng, Y. *et al*. Selective formation of metastable polymorphs in solid-state synthesis. *Sci. Adv.* **10**, eadj5431 (2024).

42. Yin, D. *et al*. Overcoming energy-scaling barriers: efficient ammonia electrosynthesis on high-entropy alloy catalysts. *Adv. Mater.* **37**, 2415739 (2025).

43. Löffler, T., Ludwig, A., Rossmeisl, J. & Schuhmann, W. What makes high-entropy alloys exceptional electrocatalysts? *Angew. Chem. Int. Ed.* **60**, 26894–26903 (2021).

44. Huang, H. *et al*. C($sp^3$)–H bond activation by perovskite solar photocatalyst cell. *ACS Energy Lett.* **4**, 203–208 (2019).

45. Li, X. *et al*. Sb-substituted $Cs_2AgBiBr_6$/g-$C_3N_4$ composite for photocatalytic C($sp^3$)–H bond activation in toluene. *Chem. Mater.* **35**, 3105–3114 (2023).

46. Bai, Z. J. *et al*. Efficient photocatalytic toluene selective oxidation over $Cs_3Bi_{1.8}Sb_{0.2}Br_9$ nanosheets: enhanced charge carriers generation and C–H bond dissociation. *Chem. Eng. Sci.* **247**, 116983 (2022).

47. Guo, Y., Chen, J., Zhao, Y. & Lou, Y. In-situ anchoring Pb-free $Cs_3Bi_2Br_9$@BiOBr quantum dots on $NH_x$-Rich silica with enhanced blue emission and satisfactory stability for photocatalytic toluene oxidation. *ChemSusChem* **15**, e202200793 (2022).

48. Zhang, H. H. *et al*. Constructing a $Cs_3Sb_2Br_9$/g-$C_3N_4$ hybrid for photocatalytic aromatic C($sp^3$)–H bond activation. *Solar RRL* **5**, 2100559 (2021).

49. Song, J. *et al*. In situ growth of lead-free perovskite $Cs_2AgBiBr_6$ on a flexible

ultrathin carbon nitride sheet for highly efficient photocatalytic benzylic C($sp^3$)−H bond activation. *Chem. Eng. J.* **453**, 139748 (2023).

50. Cui, Z. *et al*. Composite of lead-free halide perovskite $Cs_3Bi_2Br_9$ with $TiO_2$ as an efficient photocatalyst for C($sp^3$)–H bond activation. *Appl. Catal. B Environ.* **333**, 122812 (2023).

51. Li, X. *et al*. Rational atom substitution to obtain efficient, lead-free photocatalytic perovskites assisted by machine learning and DFT calculations. *Angew. Chem. Int. Ed.* **63**, e202319882 (2024).

52. Jiang, X. *et al*. In-situ assembled S-scheme heterojunction of $CsPbBr_3$ nanocrystals and $W_{18}O_{49}$ ultrathin nanowires for enhanced bifunctional photocatalysis. *Appl. Catal. B Environ.* **62**, e202315002 (2023).

53. Zhou, B. *et al*. Modulating adsorption-redox sites and charge separation of $Cs_3Bi_2Br_{9-x}$@AgBr core–shell heterostructure for selective toluene photooxidation. *ACS Energy Lett.* **9**, 1743–1752 (2024).

54. Zhang, Z. *et al*. Revealing the A-site effect of lead-free $A_3Sb_2Br_9$ perovskite in photocatalytic C($sp^3$)−H bond activation. *Angew. Chem. Int. Ed.* **59**, 18136–18139 (2020).

55. Shen, L. *et al*. Solvent-free oxidation of benzylic C($sp^3$)–H bond over $MA_3Bi_2Br_9$ perovskite photocatalyst by efficient singlet oxygen generation. *J. Catal.* **434**, 115499 (2024).

56. Rawat, B. *et al*. Utilizing the undesirable oxidation of lead-free hybrid halide perovskite nanosheets for solar-driven photocatalytic C($sp^3$)–H activation: unraveling the serendipity. *ACS Appl. Mater. Interfaces* **15**, 53604–53613 (2023).

57. Shan, T. *et al*. Efficient hole extraction to reactive oxidation sites over a $Co_3O_4/Cs_3Sb_2Br_9$ p-n heterojunction for enhanced benzylic C($sp^3$)–H bond oxidation. *Appl. Catal. B Environ.* **361**, 124602 (2025).

58. Wang, C. *et al*. Phase transition in halide double perovskites for solar-to-chemical energy conversion. *Adv. Energy Mater.* **15**, 2500921 (2025).

59. Yi, J. *et al*. High-efficiency visible-light-driven oxidation of primary C–H bonds in toluene over a $CsPbBr_3$ perovskite supported by hierarchical $TiO_2$ nanoflakes. *Nanoscale* **15**, 14584–14594 (2023).

60. Zhang, M. *et al*. Lead-free perovskite $Cs_3Bi_2Br_9$ quantum dots (QDs)/ultra-thin $W_{18}O_{49}$ nanobelts S-scheme heterojunction toward optimized photocatalytic $CO_2$ reduction coupled with toluene oxidation. *Chem. Eng. J.* **505**, 159635 (2025).

61. Bai, Z. J. *et al.* Tuning photocatalytic performance of $Cs_3Bi_2Br_9$ perovskite by g-$C_3N_4$ for C($sp^3$)–H bond activation. *Nano Res.* **16**, 6104–6112 (2023).

62. Zhan, X., Ding, C., Zhao, Q. & Fang, Y. S-scheme $TiO_2/Bi_2WO_6$ heterojunction for enhanced photocatalytic selective oxidation of toluene. *Opt. Mater.* **155**, 115860 (2024).

63. Wang, H. *et al*. Achieving high selectivity in photocatalytic oxidation of toluene on amorphous BiOCl nanosheets coupled with $TiO_2$. *J. Am. Chem. Soc.* **145**, 16852–16861 (2023).

64. Zhang, C., Qin, J., Yang, C. & Hu, Y. Sulfur-vacancy-rich $ZnS/CdIn_2S_4$ heterojunction for efficient photocatalytic selective oxidation of toluene to benzaldehyde. *J. Photochem. Photobiol. A.* **444**, 114898 (2023).

65. Li, X. *et al*. Tailoring bismuth defects in $Bi_2WO_6$ nanosheets for photocatalytic C–H activation. *J. Mater. Chem. A* 12, 11841–11847 (2024).

66. Zhou, G., Lei, B. & Dong, F. Lewis acid sites in (110) facet-exposed BiOBr promote C–H activation and selective photocatalytic toluene oxidation. *ACS Catal.* **14**, 4791–4798 (2024).

67. Cai, K. *et al*. Facile preparation of ultrathin $Bi_2MoO_6$ nanosheets for photocatalytic oxidation of toluene to benzaldehyde under visible light irradiation. *J. Solid State Chem.* **269**, 145–150 (2019).

68. Lee, S. G. *et al*. Selective photocatalytic conversion of benzyl alcohol to benzaldehyde or deoxybenzoin over ion-exchanged CdS. *Appl. Catal. B Environ.* **304**, 120967 (2022).

69. Wang, H. *et al*. Achieving high selectivity in photocatalytic oxidation of toluene on

amorphous BiOCl nanosheets coupled with $TiO_2$. *J. Am. Chem. Soc.* **145**, 16852−16861 (2023).

70. Wang, X. *et al*. Facet junction of two-dimensional metal halide perovskite for photocatalytic hydrogen evolution. *Appl. Catal. B Environ.* **365**, 124937 (2025).

71. Peng, Y. *et al*. Polar aromatic two-dimensional dion-jacobson halide perovskites for efficient photocatalytic $H_2$ evolution. *Angew. Chem. Int. Ed.* **63**, e202319882 (2024).

72. Qi, S. *et al*. Water-stable high-entropy metal-organic framework nanosheets for photocatalytic hydrogen production. *Adv. Mater.* **36**, 2403328 (2024).

73. Kresse, G. & Furthmüller J. Efficient iterative schemes for ab initio total-energy calculations using a plane-wave basis set. *Phys. Rev. B* **54**, 11169-11186 (1996).

74. Kresse, G. & Joubert, D. P. From ultrasoft pseudopotentials to the projector augmented-wave method. *Phys. Rev. B* **59**, 1758-1775 (1999).

75. Perdew, J. P., Burke, K. & Ernzerhof, M. Generalized gradient approximation made simple. *Phys. Rev. Lett.* **77**, 3865-3868 (1996).

## Acknowledgements

We thank the Research Center of Analysis and Test and the Feringa Nobel Prize Scientist Joint Research Center at East China University of Science and Technology for their assistance with the characterization. This work was also supported by the 1W1B beamline at the Beijing Synchrotron Radiation Facility.

## Funding

This work was financially supported by National Natural Science Foundation of China (22379044), Scientific Research Innovation Capability Support Project for Young Faculty (SRICSPYF-ZY2025085), Science and Technology Commission of Shanghai Municipality (23520710700), Key Program of the National Natural Science Foundation of China (22239001), Shanghai Pilot Program for Basic Research (22TQ1400100-5), Shanghai Municipal Natural Science Foundation (25ZR1401081), Fundamental Research Funds for the Central Universities, the Postdoctoral Fellowship Program and China Postdoctoral Science Fundation (BX206220), Shanghai Engineering Research Center of Hierarchical Nanomaterials (18DZ2252400), Shanghai Frontiers Science Center of Optogenetic Techniques for Cell Metabolism (Shanghai Municipal Education Commission).

## Author Contributions Statement

Y.H and S.Y. conceived the research. W. T. designed and conducted the experiments. X.L., G.C., J.Y. and H.Y. performed the theoretical calculations. W.T., X.W., Y.P., D.L. and K.X. assisted the figure preparation. W.T., D.L. and K.X. performed the structure characterization. W.T., X.W. and Y.X. contributed to the optical measurement. Y.H., S.Y. and W.T. wrote the manuscript. Y.H., S.Y., Y.P. and D.L. assisted with manuscript revision. Y.H., S.Y. and H.G.Y. provided all support needed in this work. All authors contributed to the general discussion and reviewed the paper.

## Corresponding authors

Correspondence to Yu Hou.

## Competing interests

The authors declare no competing interests.

### Additional information

**Supplementary information** Supplementary Information is available for this paper.

**Correspondence and requests for materials** should be addressed to Yu Hou.

## Supplementary Files

This is a list of supplementary files associated with this preprint. Click to download.

- SI.docx